ADVANCED MATERIALS
www.advmat.de

Porous MoO_2 Nanosheets as Non-noble Bifunctional Electrocatalysts for Overall Water Splitting

Yanshuo Jin, Haotian Wang, Junjie Li, Xin Yue, Yujie Han, Pei Kang Shen, and Yi Cui**

Electrocatalytic water splitting, including hydrogen evolution reaction (HER) and oxygen evolution reaction (OER), is now becoming increasingly important to renewable energy applications.[1] The benchmark catalysts for HER and OER are Pt-based and Ir/Ru-based compounds, respectively, however, the high cost and scarcity greatly hinder their large-scale applications.[2] Therefore the development of novel and efficient water splitting electrocatalysts based on inexpensive and earth-abundant elements to replace these noble metals is of great significance.[3] Although exciting progresses have been made,[4] there are very few electrocatalysts with high activity toward both HER and OER in the same electrolyte.[5] Such bifunctional electrocatalysts can be highly attractive because avoiding using different equipment and processes to produce different electrocatalysts could decrease the cost.[6] Because the high cost and element scarcity greatly hinder the widespread use of acid-insoluble OER electrocatalysts with reasonable activity, alkaline water splitting has emerged as a strong candidate for industrial hydrogen production.[7] Thus the non-noble bifunctional electrocatalyst for overall water splitting in alkaline media is highly attractive.[8]

Normally, an important method to improve the water splitting activity is reducing the size of the catalysts so that more catalytic active sites can be exposed.[9] Based on such key scientific method, we focused on the research of nonprecious metal catalysts with high activity and durability. MoO_2 is metallic transition metal oxide with a distorted rutile structure, which becomes a potential candidate as a non-noble metal electrocatalyst for water splitting.[10] Yu and co-workers have reported that MoO_2 and phosphorus-doped nanoporous carbon loaded on reduced graphene oxide substrates has superior performance of HER in acidic media and Liang and co-workers have shown that MoO_2–CoO coupled with a macroporous carbon hybrid electrocatalyst has good performance of OER in alkaline media.[11] However, MoO_2 for the overall water splitting in alkaline media has not been reported. The fabrication of nanostructured catalysts and then dispersing the catalysts on porous supports such as porous carbon is commonly employed. However, the possible mechanical shedding from the supporting materials would lead to catalyst deactivation and thus it is more favorable to make the catalysts themselves into porous structures.[12] The template-assisted method is a common way to synthesize porous materials, while it is complicated, expensive, and hard to grow porous materials directly on a current collector.[13] Synthesizing electrocatalytic porous materials on substrates allows direct use in device and avoids the use of binder, which may reduce effective catalytic activity because it blocks active sites and reduces gas permeability and blocks mass transfers.[14] However, it remains challenging to synthesize porous MoO_2 in a simple and facile way. Furthermore, it is a bigger challenge to synthesize porous MoO_2 directly on substrates without binder.

Herein, we report our recent efforts in developing porous MoO_2 nanosheets synthesized on nickel foam directly, which then allows direct use in device and avoids the use of binder. The porous MoO_2 was directly grown on commercial nickel foam by a wet-chemical route first and then with an annealing treatment. As an integrated non-noble high-performance electrocatalyst for overall water splitting in alkaline solution, the porous MoO_2 needs a cell voltage of only about 1.53 V to achieve current density of 10 mA cm^{-2} and maintains its activity for at least 24 h. And even the water-splitting device can be powered by an AA battery with a nominal voltage of 1.5 V at room temperature.

The porous MoO_2 nanosheets were directly grown on commercial nickel foam by a wet-chemical route first and then with an annealing treatment, as schematically elucidated in **Figure 1**a. In the first step, ammonium molybdate tetrahydrate ($(NH_4)_6Mo_7O_{24}\cdot 4H_2O$) was the molybdenum source and nickel foam substrate itself was a reductant. The introduction of sodium dodecyl sulfate (SDS) into water led to the formation of an immiscible two-phase system and a distinct oil–water interface was then constructed, with the hydrophilic $-SO_3^-$ ends arranging toward water while the hydrophobic alkyl groups away from water.[15] During the hydrothermal process,

Dr. Y. Jin, Dr. Y. Han, Prof. P. K. Shen
Collaborative Innovation Center
of Sustainable Energy Materials
Guangxi University
Nanning 530004, P. R. China
E-mail: pkshen@gxu.edu.cn
Dr. Y. Jin, J. Li, Dr. X. Yue, Dr. Y. Han, Prof. P. K. Shen
State Key Laboratory of Optoelectronic
Materials and Technologies
School of Physics and Engineering
Sun Yat-sen University
Guangzhou 510275, P. R. China
Dr. H. Wang
Department of Applied Physics
Stanford University
Stanford, CA 94305, USA
Prof. Y. Cui
Department of Materials Science and Engineering
Stanford University
Stanford, CA 94305, USA
E-mail: yicui@stanford.edu
Prof. Y. Cui
Stanford Institute for Materials and Energy Sciences
SLAC National Accelerator Laboratory
Menlo Park, CA 94025, USA

DOI: 10.1002/adma.201506314

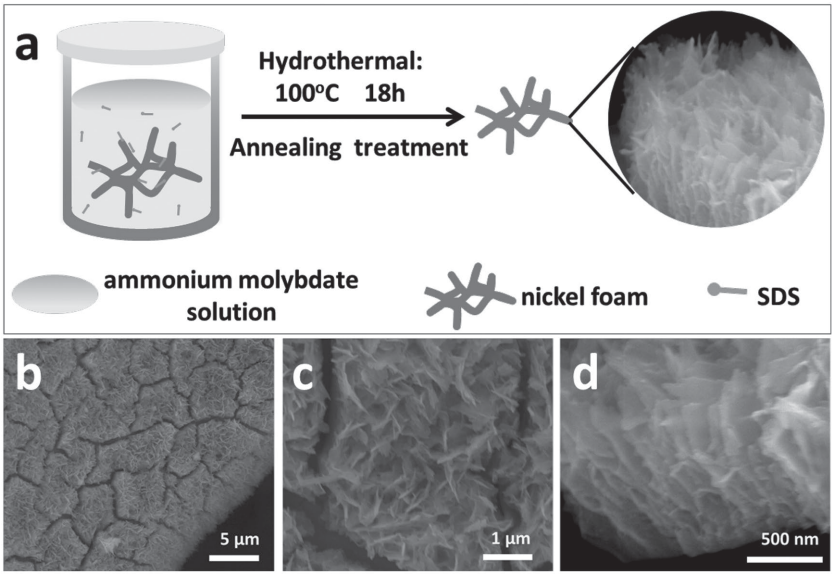

Figure 1. a) The synthetic steps of porous MoO_2 nanosheets on nickel foam directly. b,c) SEM top-view images of porous MoO_2 nanosheets synthesized on nickel foam directly at different magnifications. d) SEM side-view image of porous MoO_2 nanosheets.

the precursor nanosheets could be assembled at the oil–water interface driven by high temperature and pressure.[16] When the reaction time was gradually increased from 4 to 18 h, more precursor nanosheets were stacked up and constructed the porous precursor (Figure S1 in the Supporting Information and Figure 1c). Notably, SDS plays an important role in forming porous MoO_2 nanosheets. If SDS was not introduced into the reaction system, the microstructure consisted of thick sheets and the thickness was micrometer-sized instead of nano-sized (Figure S2, Supporting Information). Finally, the precursor became metallic MoO_2 through the annealing treatment.

Figure S3a (Supporting Information) shows the X-ray diffraction (XRD) patterns of the porous MoO_2 synthesized on nickel foam directly, the three peaks at 44.5°, 51.8°, and 76.4° originate from to the Ni foam substrate (JCPDS No. 65-2865) because the loading of MoO_2 is too low to detect its existence for XRD. After the Ni foam was removed by hydrochloric acid, the peaks assigned to monoclinic MoO_2 (JCPDS No. 32-0671) were visible (Figure S3b, Supporting Information). The Raman spectroscopy is available to measure the presence of MoO_2 directly and Figure S4 (Supporting Information) shows the Raman spectrum of the porous MoO_2, the monoclinic MoO_2 was detected with Raman bands at 200, 226, 345, 351, 456, 492, 569, and 739 cm^{-1}. Characteristic bands due to bond vibration modes of molybdenum oxide are clearly confirmed at 739 (O_2-Mo) and 569 cm^{-1} (O_1-Mo). The finger bands at 351, 345, 226, and 200 cm^{-1} can be assigned to the phonon vibration modes of MoO_2.[17] Figure S5 (Supporting Information) shows the X-ray photoelectron spectroscopy (XPS) spectra of porous MoO_2 synthesized on nickel foam directly and the various elements spectra. The Mo $3d_{5/2}$ peak of Mo^{6+} was almost coincident with the Mo $3d_{3/2}$ peak of Mo^{4+}, thus leading to the characteristic three-peak shape of Mo^{6+} and Mo^{4+}.[18] However, the amount of Mo^{6+} at the surface is much less than Mo^{4+} due to the introduction of hydrogen in the process of annealing. The element sulfur of SDS is removed during the annealing treatment and the element carbon of SDS is reduced to simple substance phase.

The scanning electron microscopy (SEM) top-view images (Figure 1b,c) show that the entire surface of the nickel foam is uniformly covered by porous MoO_2 and the porous MoO_2 is constructed by lots of nanosheets. Through the SEM side-view image (Figure 1d), the porous structure can be seen clearly. Therefore, when the porous MoO_2 nanosheets are immersed in the electrolyte, plenty of the electrolyte is initially stored in the porous ion-buffering reservoirs and, meanwhile, the nanosheets around them are covered by it, providing a quick supply and short ion-diffusion distance.[19] The skeletal structure of the Ni foam was maintained completely, thus enabling its direct use as an integrated 3D electrocatalyst for overall water splitting.

The microstructures of the porous MoO_2 were characterized by the use of transmission electron microscope (TEM). **Figure 2**a shows the TEM top-view image of the porous MoO_2 and Figure 2b shows the high resolution (HR) TEM image with interplanar distances of 0.34 and 0.48 nm, which correspond to the (011) and (100) planes of MoO_2, respectively. Figure 2c,d shows the high angle annular dark field-scanning transmission electron microscope (HAADF-STEM) images of the porous MoO_2 at different magnifications. The porous structure of MoO_2 is easily observed by HAADF-STEM, especially when compared with TEM. The sizes of the pores on the direction parallel to the Ni foam are dispersed among 5–20 nm. However, Figure 2d shows that the sizes of the pores on the direction vertical to the Ni foam are larger than that on the direction parallel to the Ni foam. In order to further study the porous structure, the Brunauer–Emmett–Teller (BET) method was used. Figure 2e shows the N_2 adsorption–desorption isotherms at 77 K. The isotherm of porous MoO_2 can be classified as a typical II isotherm with a hysteresis loop, which suggests the presence of a mesoporous structure.[20] The BET specific surface area of porous MoO_2 is 25.7 $m^2\ g^{-1}$, and pore volume of 0.101 $cm^3\ g^{-1}$ with an average pore size at 23 nm. The curve of pore size distribution (Figure 2f), determined using the density functional theory method, provides more detailed information about the pore structure of the porous MoO_2. The porous MoO_2 nanosheets have mesopore peaks and macropore peaks in the range of 10–80 nm.

Figure 3a shows the steady-state potential polarization curves (for details of porous MoO_2, see Figure S6a,b, Supporting Information) of Ni foam, commercial 46.7% Pt/C deposited on Ni foam (TKK, Japan, loading: 0.5 mg cm^{-2}), compact MoO_2 (for additional SEM image, see Figure S7, Supporting Information) synthesized on nickel foam directly (MoO_2 loading: ≈3.4 mg cm^{-2}), and porous MoO_2 synthesized on nickel foam directly (MoO_2 loading: ≈2.9 mg cm^{-2}) in N_2-saturated 1 M KOH solution at 25 °C for HER and OER. At left, porous MoO_2 is significantly active for the HER with onset potential of almost 0 V, and additional negative potential leads to rapid increase in the cathodic current. In addition, porous MoO_2

Adv. Mater. 2016,
DOI: 10.1002/adma.201506314

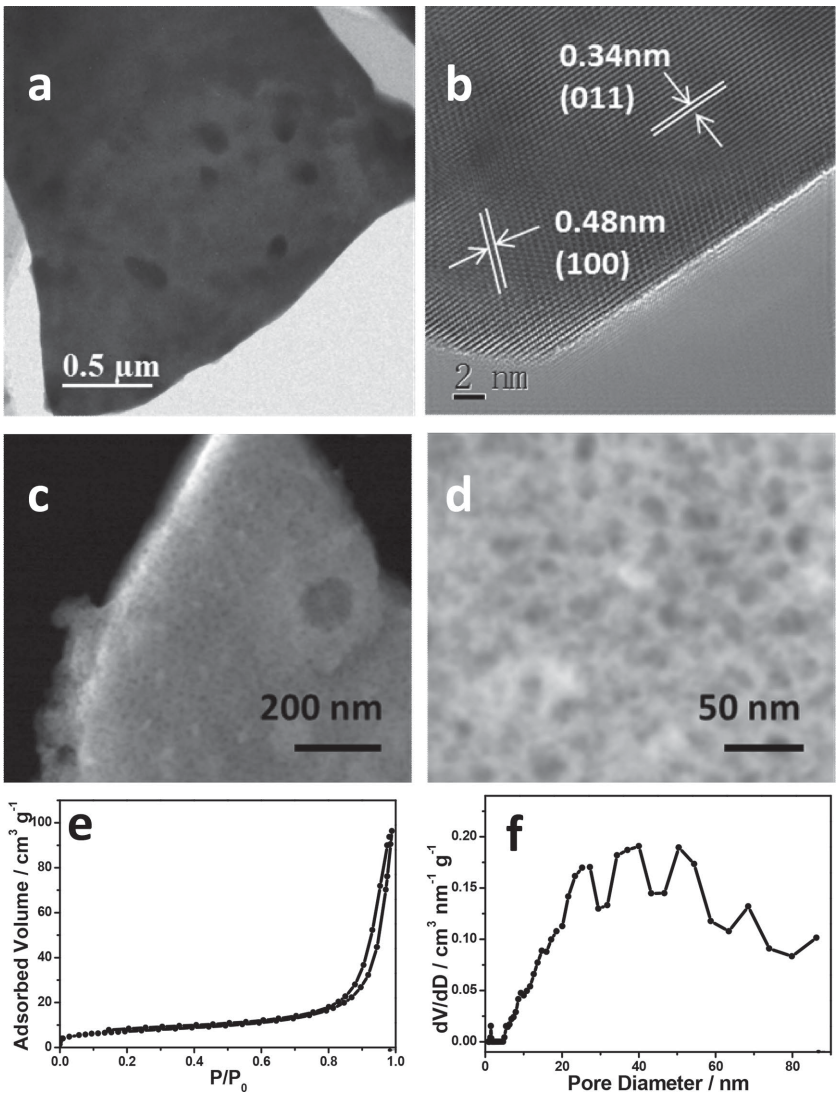

Figure 2. a) TEM top-view image of the porous MoO_2 nanosheets. b) HRTEM image of the porous MoO_2. c,d) HAADF-STEM top-view images of the porous MoO_2 at different magnifications. e) N_2 adsorption–desorption isotherms of porous MoO_2. f) The corresponding pore size distribution of porous MoO_2.

needs overpotentials of only about 27 and 40 mV to achieve current densities of −10 and −20 mA cm^{-2}, respectively. The Tafel slopes (Figure S8, Supporting Information) are 117, 29, 116, and 41 mV dec^{-1} for Ni foam, Pt/C, compact MoO_2, and porous MoO_2, respectively. The Tafel slope of porous MoO_2 is only 41 mV dec^{-1}, implying a rapid HER rate and a Heyrovsky–Volmer mechanism with electrochemical desorption of hydrogen as the rate-limiting step.[21] The linear sweep voltammetry curve of the porous MoO_2 in a larger potential window is shown in Figure S9 (Supporting Information). The sufficiently low onset potential and Tafel slope indicate an excellent HER activity and it is even competitive with commercial Pt catalysts. The Faradic efficiency (FE) was calculated by comparing the amount of experimentally quantified gas with theoretically calculated gas. As shown in Figure S10 (Supporting Information), the FE is close to 100 % for HER. The durability of porous MoO_2 for HER was also examined. As shown in Figure S11a (Supporting Information), the porous MoO_2 exhibits a fairly stable performance within the accelerated degradation measurement for 1000 cyclic voltammetry (CV) cycles. Figure S11b (Supporting Information) shows the time-dependent current density curve for porous MoO_2 under steady-state potential of 100 mV versus RHE (without iR correction) for 12 h. After a long period of time, the current density only slightly degrades, indicating that the porous MoO_2 has superior stability in the long-term electrochemical process. The XRD pattern (Figure S12, Supporting Information), SEM image (Figure S13, Supporting Information), and XPS spectra (Figure S14, Supporting Information) after HER show the robust and stable natures of the porous MoO_2 for HER. At right, porous MoO_2 is significantly active for the OER with onset potential of ≈1.43 V. In addition, porous MoO_2 needs potentials of only about 1.49 and 1.51 V to achieve current densities of 10 and 20 mA cm^{-2}, respectively. Figure S15 (Supporting Information) shows the Tafel slope of porous MoO_2 (54 mV dec^{-1}) is smaller than that of Ni foam (113 mV dec^{-1}), Pt/C (61 mV dec^{-1}), and compact MoO_2 (88 mV dec^{-1}), implying a more rapid OER rate for porous MoO_2. Figure S16 (Supporting Information) shows that the redox peak current of porous MoO_2 decreases when scan rate decreases, thus steady-state polarization curve can avoid the interference of redox current. As shown in Figure S16b (Supporting Information), we can also confirm that the onset potential is ≈1.43 V for OER. In addition, the FE for OER is close to 100 % (Figure S17, Supporting Information). The durability of porous MoO_2 for OER was also examined. As shown in Figure S18a (Supporting Information), the porous MoO_2 exhibits a fairly stable performance within the accelerated degradation measurement for 3000 CV cycles. Figure S18b (Supporting Information) shows the time-dependent potential curves of porous MoO_2 under steady-state current density of 5 mA cm^{-2} and 20 mA cm^{-2}. After a long period of time, the potential is nearly invariable, indicating that the porous MoO_2 has superior stability in the long-term electrochemical process. The XRD pattern (Figure S19, Supporting Information) and SEM image (Figure S20, Supporting Information) after OER show the robust and stable natures of the porous MoO_2 for OER. As shown in Figure S21 (Supporting Information), Mo^{4+} has changed into Mo^{6+} after OER.

Given that porous MoO_2 is an active and stable electrocatalyst toward both HER and OER in strongly basic media, we made an electrolyzer in a two-electrode setup using porous MoO_2 as both anode and cathode to go a step closer to the real application. According to the charge conservation and $I = Q/t$, the cathode current (I_c) and the anode current (I_a) are equal in

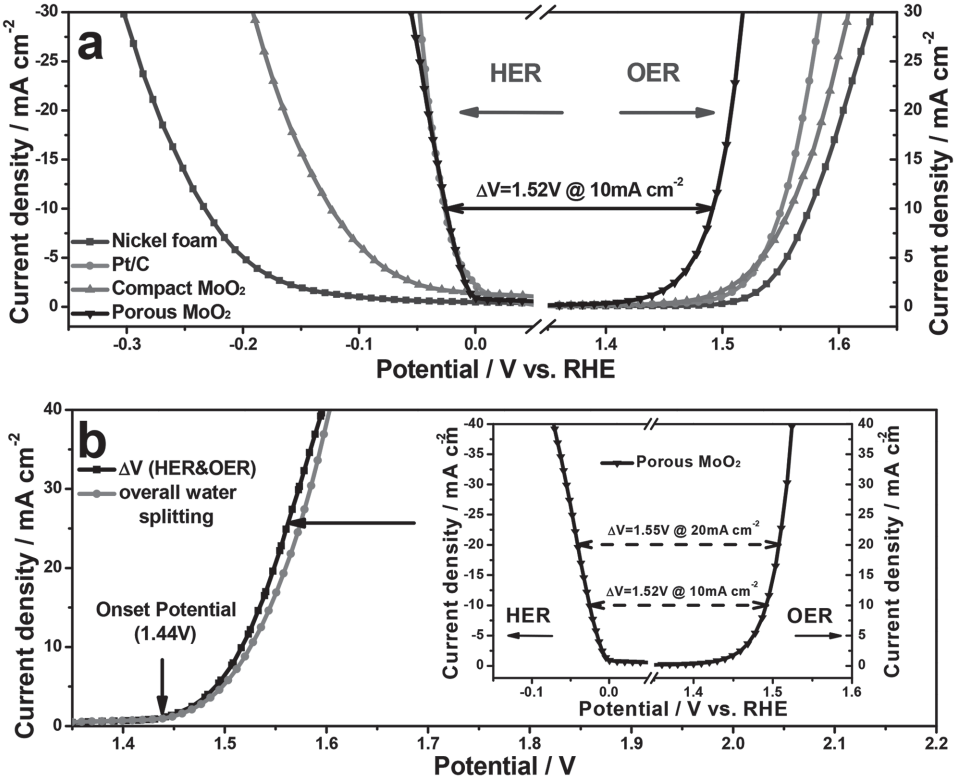

Figure 3. a) Steady-state polarization curves of Ni foam, commercial Pt/C, compact MoO_2, and porous MoO_2 in 1 M KOH for HER and OER. b) Steady-state polarization curve for overall water splitting of porous MoO_2 in a two-electrode configuration and the voltage difference between HER and OER. (Inset: Steady-state polarization curves of porous MoO_2 for HER and OER.)

amount but opposite in sign. In addition, when the cathode surface (S_c) is equal to the anode surface (S_a), the cathode current density (j_c) and the anode current density (j_a) are equal in amount but opposite in sign. Therefore, the voltage for overall water splitting should be equal to the voltage difference (ΔV) between HER and OER at the same current density in amount. Further, the onset potential of overall water splitting should be equal to the voltage difference (ΔV) between the onset potential of HER and OER. As shown in Figure 3b, the steady-state polarization curve (for details see Figure S6c, Supporting Information) for overall water splitting of porous MoO_2 and the voltage difference (ΔV) between HER and OER are basically the same. Meanwhile the onset potential (1.44 V) is close to the voltage difference (ΔV) between the onset potential of HER (near-zero) and OER (1.43 V). Onset potential is a very important parameter in judging intrinsic activities of the electrocatalysts, especially in the field of water splitting. Due to the low onset potential of HER and OER, the onset potential of porous MoO_2 for overall water splitting is low and comparable to the state-of-the-art overall water splitting catalysts (Table S1, Supporting Information).[5,6,8,9,22]

Figure 4a shows the steady-state potential polarization curves of Ni foam, commercial 46.7% Pt/C deposited on Ni foam, compact MoO_2 synthesized on nickel foam directly, and porous MoO_2 synthesized on nickel foam directly for overall water splitting. Compared with Ni foam, commercial Pt/C, and compact MoO_2, porous MoO_2 exhibits excellent performance for alkaline water electrolyzer with the need of a cell voltage of only 1.53 V to afford 10 mA cm^{-2} water-splitting current in 1.0 M KOH. Remarkably, the catalytic activity of porous MoO_2 is comparable to the state-of-the-art overall water splitting catalysts (Table S1, Supporting Information).[5,6,8,9,22] Such water electrolysis could be powered by a single-cell AA battery with a nominal voltage of ≈1.5 V at room temperature (Figure 4b and Figure S22, Supporting Information; and see Movie S1 in the Supporting Information for a movie of water electrolysis by an AA battery). As we know, those electrons move to the cathode from the anode, providing electrical power and producing H_2 at the cathode and O_2 at the anode. We also tested the long-term stability of this system for 24 h in 1.0 M KOH solution at 25 °C. The potential only slightly degrades (Figure 4c), indicating that the porous MoO_2 has superior stability in the long-term electrochemical process.

In contrast, without porous morphology, the compact MoO_2 shows much lower activity for HER, OER, and overall water splitting. The roughness factor (RF) is used to determine the amount of catalytically active sites and defined as the ratio of the electrochemically active surface area to the geometric surface area of the electrode. The electrochemically active surface area can be estimated from the electrochemical double-layer capacitance, which is calculated from the CV curves measured in a non-Faradaic region at different scan rates (for calculation details see Figure S23, Supporting Information). Indeed, the electrochemical double-layer capacitance of porous MoO_2 (422 mF cm^{-2}) is considerably larger than that of compact MoO_2 (31 mF cm^{-2}), which means the RF of porous MoO_2

Adv. Mater. 2016,
DOI: 10.1002/adma.201506314

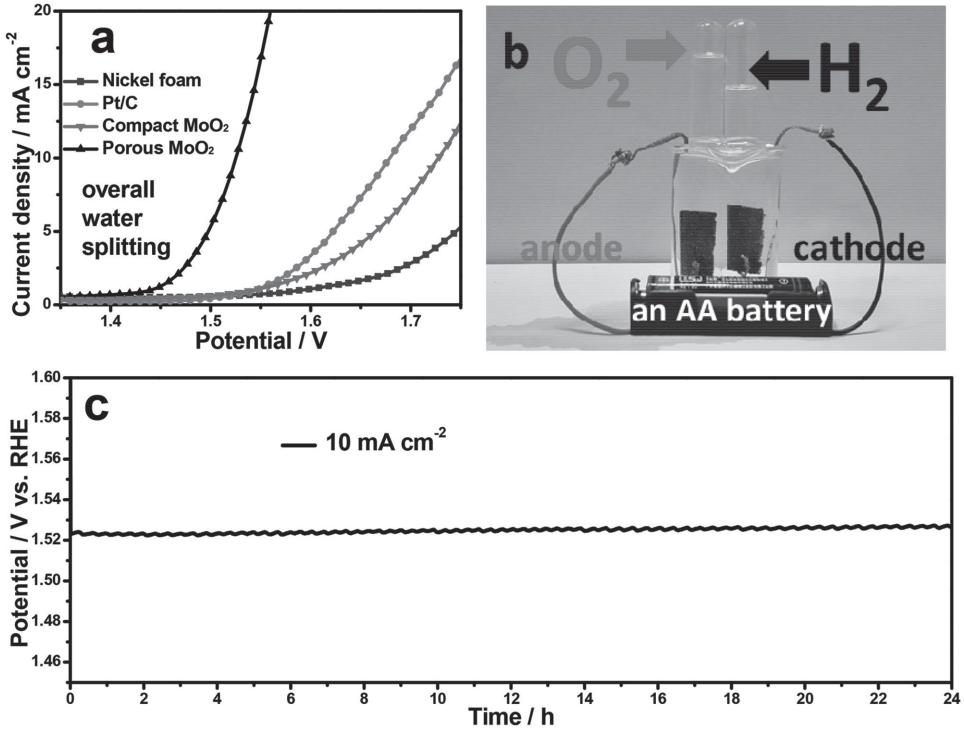

Figure 4. a) Steady-state polarization curves for overall water splitting of Ni foam, commercial Pt/C, compact MoO_2, and porous MoO_2 in a two-electrode configuration. b) Demonstration of water-splitting device powered by an AA battery with a nominal voltage of ≈1.5 V. c) Chronopotentiometric curve of water electrolysis for porous MoO_2 in a two-electrode configuration with constant current density of 10 mA cm^{-2}.

is considerably larger than that of compact MoO_2. Thus, the superior overall water splitting electrocatalytic performance of porous MoO_2 could be attributed to the high surface area contributed by porous nanostructuring, there are correspondingly many active sites exposed for both HER and OER. In addition, synthesizing electrocatalytic porous MoO_2 nanosheets on Ni foam avoids the use of binder. As we know, binder would reduce effective catalytic activity because it blocks active sites and reduces gas permeability and blocks mass transfers.[14]

In order to avoid the potential synergistic effect of Ni foam and porous MoO_2 or the potential formation of NiMo (or NiMo oxides) at the interfaces between the nickel foam and porous MoO_2 during the annealing treatment,[23] porous MoO_2 was grown on carbon paper. Figure S24 (Supporting Information) shows the XRD pattern of the porous MoO_2/carbon paper, and the peaks assigned to monoclinic MoO_2 (JCPDS No. 32-0671) were visible. Figure S25 (Supporting Information) shows the SEM image of the porous MoO_2/carbon paper and elemental mapping of C, O, and Mo. Figure S26 (Supporting Information) shows the polarization curves of the porous MoO_2/carbon paper for HER and OER in 1 M KOH. The onset potential for HER and OER of porous MoO_2/carbon paper is similar to that of porous MoO_2/Ni foam. Thus whether Ni foam or carbon paper is used as the substrate, the porous MoO_2 has similar high activity for HER and OER. However, the current density for HER and OER of porous MoO_2/carbon paper is less than that of porous MoO_2/Ni foam. This is because the electrochemical double-layer capacitance of porous MoO_2/Ni foam (422 mF cm^{-2}) is larger than that of MoO_2/carbon paper (57 mF cm^{-2}; Figure S27, Supporting Information), which means the electrochemically active surface area of MoO_2/Ni foam is considerably larger than that of MoO_2/carbon paper. Thus the 3D structure of Ni foam enables it to load more electrocatalysts. Figures S28 and S29 (Supporting Information) show the SEM images of the porous MoO_2/carbon paper and elemental mappings of C, O, and Mo post HER and OER, which show the robust and stable natures of the porous morphology.

In summary, the porous MoO_2 nanosheets were directly grown on commercial nickel foam without binder by a simple wet-chemical route first and then with an annealing treatment. The porous MoO_2 shows much higher activity toward both HER and OER than the compact MoO_2, which could be attributed to the higher surface area and more active sites contributed by porous nanostructuring. As an active and stable bifunctional electrocatalyst for overall water splitting, the porous MoO_2 needs a cell voltage of only about 1.53 V to achieve current density of 10 mA cm^{-2} and maintains its activity for at least 24 h in a two-electrode configuration and 1 M KOH. Even the water-splitting device can be powered by an AA battery with a nominal voltage of 1.5 V at room temperature. The porous MoO_2 is one of the best high-performance bifunctional electrocatalysts for overall water splitting and this work offers an attractive cost-effective catalytic material toward overall water splitting applications.

Supporting Information

Supporting Information is available from the Wiley Online Library or from the author.

Acknowledgements

This work was supported by the Major International (Regional) Joint Research Project (51210002), the National Basic Research Program of China (2015CB932304), and the Natural Science Foundation of Guangdong province (2015A030312007). P.K.S. acknowledges the support from the Danish project of Initiative toward Non-precious Metal Polymer Fuel Cells (4106-000012B).

Received: December 18, 2015
Revised: January 30, 2016
Published online:

[1] a) X. Zou, Y. Zhang, *Chem. Soc. Rev.* **2015**, *44*, 5148; b) T. E. Mallouk, *Nat. Chem.* **2013**, *5*, 362.
[2] a) D. Voiry, H. Yamaguchi, J. Li, R. Silva, D. C. B. Alves, T. Fujita, M. Chen, T. Asefa, V. B. Shenoy, G. Eda, M. Chhowalla, *Nano lett.* **2013**, *12*, 6222; b) Y. Jiao, Y. Zheng, M. Jaroniec, S. Z. Qiao, *Chem. Soc. Rev.* **2015**, *44*, 2060.
[3] a) D. Chen, C. Chen, Z. M. Baiyee, Z. Shao, F. Ciucci, *Chem. Rev.* **2015**, *115*, 9869; b) C. G. Morales-Guio, L. Stern, X. Hu, *Chem. Soc. Rev.* **2014**, *43*, 6555.
[4] a) D. Voiry, H. Yamaguchi, J. Li, R. Silva, D. C. B. Alves, T. Fujita, M. Chen, T. Asefa, V. B. Shenoy, G. Eda, M. Chhowalla, *Nat. Mater.* **2013**, *12*, 850; b) J. Kibsgaard, Z. Chen, B. N. Reinecke, T. F. Jaramillo, *Nat. Mater.* **2012**, *11*, 963; c) M. Gong, Y. Li, H. Wang, Y. Liang, J. Z. Wu, J. Zhou, J. Wang, T. Regier, F. Wei, H. Dai, *J. Am. Chem. Soc.* **2015**, *135*, 8452; d) H. Wang, Z. Lu, S. Xu, D. Kong, J. J. Cha, G. Zheng, P. Hsu, K. Yan, D. Bradshaw, F. B. Prinz, Y. Cui, *Proc. Natl. Acad. Sci. USA* **2013**, *110*, 19701; e) Z. Lu, H. Wang, D. Kong, K. Yan, P. Hsu, G. Zheng, H. Yao, Z. Liang, X. Sun, Y. Cui, *Nat. Commun.* **2015**, *5*, 4345; f) J. Xie, H. Zhang, S. Li, R. Wang, X. Sun, M. Zhou, J. Zhou, X. W. D. Lou, Y. Xie, *Adv. Mater.* **2013**, *25*, 5807; g) X. Sun, J. Dai, Y. Guo, C. Wu, F. Hu, J. Zhao, X. Zeng, Y. Xie, *Nanoscale* **2014**, *6*, 8359; h) L. Liao, S. Wang, J. Xiao, X. Bian, Y. Zhang, M. D. Scanlon, X. Hu, Y. Tang, B. Liu, H. H. Girault b, *Energy Environ. Sci.* **2014**, *7*, 387; i) H. Vrubel, X. Hu, *Angew. Chem.* **2012**, *124*, 12875; j) *Angew. Chem. Int. Ed.* **2012**, *51*, 12703.
[5] a) L. Stern, L. Feng, F. Song, X. Hu, *Energy Environ. Sci.* **2015**, *8*, 2347; b) H. Wang, H. Lee, Y. Deng, Z. Lu, P. Hsu, Y. Liu, D. Lin, Y. Cui, *Nat. Commun.* **2015**, *6*, 7261.
[6] a) C. Tang, N. Cheng, Z. Pu, W. Xing, X. Sun, *Angew. Chem.* **2015**, *127*, 9483; b) *Angew. Chem. Int. Ed.* **2015**, *54*, 9351.
[7] M. S. Burke, M. G. Kast, L. Trotochaud, A. M. Smith, S. W. Boettcher, *J. Am. Chem. Soc.* **2015**, *137*, 3638.
[8] a) M. Ledendecker, S. K. Calderón, C. Papp, H. Steinrück, M. Antonietti, M. Shalom, *Angew. Chem.* **2015**, *127*, 12538; b) *Angew. Chem. Int. Ed.* **2015**, *54*, 12361.
[9] Y. Yang, H. Fei, G. Ruan, M. Tour, *Adv. Mater.* **2015**, *27*, 3175.
[10] Y. Jin, P. K. Shen, *J. Mater. Chem. A* **2015**, *3*, 20080.
[11] a) Y. Tang, M. Gao, C. Liu, S. Li, H. Jiang, Y. Lan, M. Han, S. Yu, *Angew. Chem.* **2015**, *127*, 13120; b) *Angew. Chem. Int. Ed.* **2015**, *54*, 12928; b) B. B. Li, Y. Q. Liang, X. J. Yang, Z. D. Cui, S. Z. Qiao, S. L. Zhu, Z. Y. Li, K. Yin, *Nanoscale* **2015**, *7*, 16704.
[12] a) C. H. Bartholomew, *Appl. Catal. A* **2001**, *212*, 17; b) D. Kong, H. Wang, Z. Lu, Y. Cui, *J. Am. Chem. Soc.* **2014**, *136*, 4897.
[13] Y. Shi, B. Guo, S. A. Corr, Q. Shi, Y. Hu, K. R. Heier, L. Chen, R. Seshadri, G. D. Stucky, *Nano Lett.* **2009**, *9*, 4215.
[14] G. Sasikumar, J. W. Ihm, H. Ryu, *Electrochim. Acta* **2004**, *50*, 601.
[15] J. Ni, Y. Zhao, L. Li, L. Mai, *Nano Energy* **2015**, *11*, 129.
[16] S. Hu, X. Wang, *J. Am. Chem. Soc.* **2008**, *130*, 8126.
[17] M. Dieterle, G. Mestl, *Phys. Chem. Chem. Phys.* **2002**, *4*, 822.
[18] X. Wang, Y. Xiao, J. Wang, L. Sun, M. Cao, *J. Power Sources* **2015**, *274*, 142.
[19] Y. Li, Z. Li, P. K. Shen, *Adv. Mater.* **2013**, *25*, 2474.
[20] J. Cheng, J. Zhu, X. Wei, P. K. Shen, *J. Mater. Chem. A* **2015**, *3*, 10026.
[21] a) Y. Li, H. Wang, L. Xie, Y. Liang, G. Hong, H. Dai, *J. Am. Chem. Soc.* **2011**, *133*, 7296; b) M. Xu, L. Han, Y. Han, Y. Yu, J. Zhai, S. Dong, *J. Mater. Chem. A* **2015**, *3*, 21471.
[22] a) L. Feng, G. Yu, Y. Wu, G. Li, H. Li, Y. Sun, T. Asefa, W. Chen, X. Zou, *J. Am. Chem. Soc.* **2015**, *137*, 14023; b) N. Jiang, B. You, M. Sheng, Y. Sun, *Angew. Chem.* **2015**, *127*, 6349; c) *Angew. Chem. Int. Ed.* **2015**, *54*, 6251.
[23] a) J. K. Huot, M. L. Trudeau, R. Schulz, *J. Electrochem. Soc.* **1990**, *137*, 1408; b) J. R. McKone, B. F. Sadtler, C. A. Werlang, N. S. Lewis, H. B. Gray, *ACS Catal.* **2013**, *3*, 166; c) W. F. Chen, K. Sasaki, C. Ma, A. I. Frenkel, N. Marinkovic, J. T. Muckerman, Y. Zhu, R. R. Adzic, *Angew. Chem.* **2012**, *124*, 6235; d) *Angew. Chem. Int. Ed.* **2012**, *51*, 6131.